



## In-situ determination of the kinetics and mechanisms of nickel adsorption by nanocrystalline vernadite

Sylvain Grangeon, Alejandro Fernandez-Martinez, Francis Claret, Nicolas C.M. Marty, Christophe Tournassat, Fabienne Warmont, Alexandre Gloter

### ► To cite this version:

Sylvain Grangeon, Alejandro Fernandez-Martinez, Francis Claret, Nicolas C.M. Marty, Christophe Tournassat, et al.. In-situ determination of the kinetics and mechanisms of nickel adsorption by nanocrystalline vernadite. Chemical Geology, 2017, 459, pp.24 - 31. 10.1016/j.chemgeo.2017.03.035 . hal-01849472

**HAL Id: hal-01849472**

**<https://brgm.hal.science/hal-01849472>**

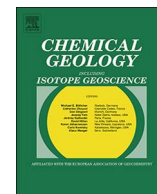
Submitted on 26 Mar 2021

**HAL** is a multi-disciplinary open access archive for the deposit and dissemination of scientific research documents, whether they are published or not. The documents may come from teaching and research institutions in France or abroad, or from public or private research centers.

L'archive ouverte pluridisciplinaire **HAL**, est destinée au dépôt et à la diffusion de documents scientifiques de niveau recherche, publiés ou non, émanant des établissements d'enseignement et de recherche français ou étrangers, des laboratoires publics ou privés.



Distributed under a Creative Commons Attribution - NoDerivatives 4.0 International License



# In-situ determination of the kinetics and mechanisms of nickel adsorption by nanocrystalline vernadite



Sylvain Grangeon<sup>a,\*</sup>, Alejandro Fernandez-Martinez<sup>b,c</sup>, Francis Claret<sup>a</sup>, Nicolas Marty<sup>a</sup>,  
Christophe Tournassat<sup>a</sup>, Fabienne Warmont<sup>d</sup>, Alexandre Gloter<sup>e</sup>

<sup>a</sup> BRGM, 3 avenue Claude Guillemin, 45060 Orléans Cedex 2, France

<sup>b</sup> University Grenoble Alpes, ISTERre, 38041 Grenoble, France

<sup>c</sup> CNRS, ISTERre, 38041 Grenoble, France

<sup>d</sup> ICMN-CNRS-Université d'Orléans, 1b rue de la Férollerie, 45071 Orléans Cedex 2, France

<sup>e</sup> Laboratoire de Physique des Solides, Université Paris-Sud, CNRS UMR 8502, 91405 Orsay Cedex, France

## ARTICLE INFO

### Keywords:

Manganese oxide

Vernadite

Birnessite

Pair distribution function

Nickel

Transmission electron microscopy

## ABSTRACT

In-situ kinetics and mechanisms of  $\text{Ni}^{2+}$  uptake by synthetic vernadite were determined at pH 5.8 and  $I = 0.1$  M NaCl using wet chemistry, atomic-resolution scanning transmission electron microscopy coupled with electron energy loss spectroscopy (STEM-EELS) and synchrotron high-energy X-ray scattering (HEXS) in both the Bragg-rod and pair distribution function formalisms. The structural formula of the initial solids was  $\text{TCMn}_{0.05}^{3+}\text{Na}^{+}_{0.23}(\text{H}_2\text{O})_{0.69}\text{H}^{+}_{0.06}[(\text{Mn}^{4+}_{0.86}\text{Mn}^{3+}_{0.04}\text{vac}_{0.1})\text{O}_2]$ , where species under brackets form the layer having “vac” layer vacancies, and where other species are present in the interlayer, with TC standing for “triple-corner sharing” configuration. According to HEXS and STEM-EELS, adsorbed  $\text{Ni}^{2+}$  adopted mainly a TC configuration, and had a Debye-Waller factor about four times higher than layer Mn. Steady-state was reached after  $\sim 2.2$  h of contact time, and the final structural formula of the solid was  $\text{TCNi}^{2+}_{0.12}\text{TCMn}^{3+}_{0.05}\text{Na}^{+}_{0.12}\text{H}_2\text{O}_{0.36}\text{H}^{+}_{0.01}[(\text{Mn}^{4+}_{0.87}\text{vac}_{0.13})\text{O}_2]$ . Atomic-scale imaging of the solids also evinced the presence of minor Ni adsorbed at the crystal edge. The retention coefficient  $R_D = 10^{3.76 \pm 0.06} \text{ L kg}^{-1}$ , computed from PDF data modelling and solution chemistry results, was in agreement with those available in the literature.

## 1. Introduction

Vernadite, a manganese (Mn) oxide, is ubiquitous in the environment, being found as nodules and coatings in soil and sediments or as rock varnishes in deserts and polar and temperate regions (Bargar et al., 2009; Burns and Burns, 1977; Chukhrov et al., 1985; Dorn, 1991; Dorn et al., 1992; Dorn and Oberlander, 1981; Exon et al., 2002; Fuller and Bargar, 2014; Glover, 1977; Manceau et al., 2003, 2004; Marcus et al., 2004; Palumbo et al., 2001; Potter and Rossman, 1979). In surficial environments, vernadite precipitation by oxidation of aqueous  $\text{Mn}^{2+}$  in the presence of bacteria, fungi, and higher living forms (Grangeon et al., 2010; Lanson et al., 2008; Tani et al., 2003; Villalobos et al., 2003; Webb et al., 2005) is faster than abiotic oxidation catalysed by mineral surfaces by orders of magnitude (e.g. Hastings and Emerson, 1986; Tebo et al., 2004). Vernadite structure consists in the turbostratic stacking of layers made of  $(\text{Mn}^{4+}\text{O}_6)^{8-}$  octahedra connected through their edges and separated from each other by hydrated interlayer cations (Giovannoli, 1980). These layers contain isomorphic substitu-

tions of  $\text{Mn}^{4+}$  by cations of lower valences (e.g.,  $\text{Mn}^{3+}$ ,  $\text{Ni}^{2+}$ ,  $\text{Co}^{2+}$ ) and/or layer vacancies (Grangeon et al., 2008; Lanson et al., 2008; Villalobos et al., 2006), which induce a layer charge deficit reported to reach values as high as 1.6 valence unit (v.u.) per layer octahedron (Lanson et al., 2008). The layer charge deficit created by substituted octahedron (1 or 2 v.u. for trivalent and divalent octahedral cations respectively) is mostly compensated for by adsorbed hydrated cations forming outer-sphere complexes (e.g.  $\text{Na}^+$ ,  $\text{Ca}^{2+}$ ), while the layer charge deficit created by vacant Mn site (4 v.u.) is most frequently compensated for by adsorbed cations forming inner-sphere complexes above layer vacancies, in a triple-corner sharing (TC) configuration (e.g.,  $\text{Cu}^{2+}$ ,  $\text{Mn}^{3+}$ ,  $\text{Pb}^{2+}$ ,  $\text{Zn}^{2+}$  - Grangeon et al., 2012; Lanson et al., 2000, 2002b; Manceau et al., 2014; Peña et al., 2015). In addition, vernadite is nanocrystalline (Bargar et al., 2009) and its small particles have thus a large edge specific surface area, which bears a significant density of amphoteric reactive sites (Simanova et al., 2015). For all of these reasons, vernadite has high reactivity towards many trace elements and the geochemical cycle of many metals, rare-earth

\* Corresponding author.

E-mail address: [s.grangeon@brgm.fr](mailto:s.grangeon@brgm.fr) (S. Grangeon).

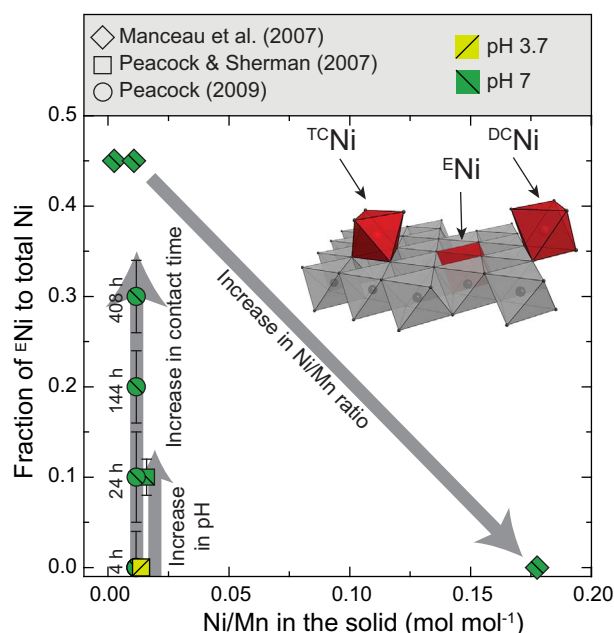


Fig. 1. Dependency of the abundance of  $^{58}\text{Ni}$  to various environmental factors. Blue, yellow and green colours indicate that studies were conducted respectively at pH 3.7, 7 and 8. From left to right, arrows highlight the dependency of the abundance of  $^{58}\text{Ni}$  on an increase in contact time, on Ni/Mn ratio, and on pH. The structure model drawn on the right schematizes the different configurations that Ni can adopt upon contact with vernadite. Red spheres and red octahedra materialize Ni and its coordination sphere respectively, while black spheres and grey octahedra materialize layer Mn and its coordination sphere respectively. (For interpretation of the references to colour in this figure legend, the reader is referred to the web version of this article.)

elements and actinides is controlled, or at least influenced, by vernadite in certain soils, freshwater and marine sediments (Koschinsky and Halbach, 1995; Manceau et al., 2000, 2004, 2007a; Marcus et al., 2004; Peacock and Moon, 2012; Peacock and Sherman, 2007a; Takahashi et al., 2007). Amongst metals,  $\text{Ni}^{2+}$  is of special interest, because of its toxicity (Kasprzak et al., 2003; Wang and Wang, 2008; Weng et al., 2004) and of its wide use in industrial processes and manures for agriculture (Nicholson et al., 2003).

Upon contact with vernadite,  $\text{Ni}^{2+}$  can adopt three main configurations (inset in Fig. 1): adsorbed at the particle edge in a double corner sharing configuration ( $^{\text{DC}}\text{Ni}$ ), located above layer vacancies in a triple corner-sharing configuration ( $^{\text{TC}}\text{Ni}$ ), or incorporated within the layer ( $^{\text{E}}\text{Ni}$ ) (Grangeon et al., 2008; Manceau et al., 2007b; Peacock, 2009; Peacock and Sherman, 2007a,b; Peña et al., 2010).  $^{\text{E}}\text{Ni}$  is favoured when surface coverage (i.e., Ni/Mn ratio) is low, when the pH of the equilibrium solution is alkaline, and when contact time between solution and vernadite is long (Fig. 1).

In many environmental compartments, the interaction between  $\text{Ni}^{2+}$  in solution and vernadite takes place in open chemical system where contact time is limited. These include streams, rivers, or the critical zone in soils. The kinetics of  $\text{Ni}^{2+}$ -vernadite interactions which certainly greatly influence the capacity of vernadite to uptake  $\text{Ni}^{2+}$  in these systems remain however largely undocumented. The importance of quantifying the kinetics of trace elements interaction with vernadite was discussed by Lopano and coworkers (Lopano et al., 2009, 2011) who studied the rates of exchange of  $\text{Na}^+$  by  $\text{Ba}^{2+}$ ,  $\text{Cs}^+$  and  $\text{K}^+$  on synthetic birnessite, a three-dimensionally ordered phyllosilicate. Exchange processes were fast as samples reached equilibrium in the first hour of contact time, but only adsorption in the interlayer as outer-sphere complex could be probed because the authors used a birnessite with orthogonal layer symmetry, which contains very little layer vacancies, thus hindering the formation of inner-sphere complexes (Lanson et al., 2002a). The relevance of using such birnessite variety as a proxy for naturally-occurring vernadite may be questioned as this

latter generally has hexagonal layer symmetry, as a result of a lower abundance of layer  $\text{Mn}^{3+}$  and of the frequent presence of layer vacancies (Bargar et al., 2009; Bodei et al., 2007; Lanson et al., 2000; Manceau et al., 2014; Peacock and Sherman, 2007a; Wegorzewski et al., 2015).

This study aims at elucidating the mechanisms and quantifying the kinetics of  $\text{Ni}^{2+}$  uptake by vernadite. Synchrotron high-energy X-ray scattering followed by analysis in both Bragg-rod and pair distribution function formalisms made it possible to monitor sorption processes as a function of reaction time. These processes were further confirmed with atomic-resolution scanning transmission electron microscopy (STEM) coupled with energy electron-loss spectroscopy (EELS).

## 2. Materials and methods

### 2.1. Synthesis of the sample and chemical characterization

Synthetic vernadite ( $\delta\text{-MnO}_2$ ) was synthesized using the redox method (Villalobos et al., 2003). Briefly, a solution made of  $\sim 40\text{ g KMnO}_4$  dissolved in  $\sim 1.3\text{ L}$  of deionized water was added to a solution made of  $28\text{ g NaOH}$  dissolved in  $1.4\text{ L}$  of deionized water. Then, a solution made of  $\sim 75\text{ g MnCl}_2\cdot 4\text{H}_2\text{O}$  was added, leading to the precipitation of synthetic vernadite which was separated from the solution by 10 series of centrifugation and Na saturation using a  $1\text{ M NaCl}$  solution. The obtained Na-saturated synthetic vernadite was freeze-dried. An aliquot of the powder was used for the determination of the average Mn oxidation state (Mn AOS), using a potentiometric method (Grangeon et al., 2012).

### 2.2. High-energy X-ray scattering

High-energy X-ray scattering (HEXS) experiments were performed at station ID22 from the European Radiation Synchrotron Facility (ESRF, Grenoble, France), using energy of  $69.9\text{ keV}$  and a Perkin Elmer XRD 1611CP3 flat detector. A polyimide capillary (diameter of  $1.6\text{ mm}$ ) was filled with synthetic vernadite, sealed on its two extremities using a frit-in-a-ferrule system (IDEX Health & Science), and fixed in its measurement position. It was connected on one side to a peristaltic pump, used to flow the  $\text{Ni}^{2+}$  solution through the capillary, and to the other side to a waste container, using silicon tubing. A scheme of a similar set-up is available elsewhere (Marty et al., 2015). Flow rate was set to  $20\text{ mL h}^{-1}$ . The input solution had a pH of 5.8 and contained  $2 \times 10^{-4}\text{ M NiCl}_2$  in a  $0.1\text{ M NaCl}$  ionic background, so as to remain in chemical conditions comparable to previously published data (Tonkin et al., 2004). Recording of data started as soon as the solution was allowed to flow. An acquisition step consisted in the successive recording of 20 frames (5 s collection time each) and lasted 5 min, because of the need to record detector's dark current. Each acquisition step was separated from the next one by a dwell time of 2 min. The 20 frames acquired at each step were averaged and integrated using the pyFAI package (Ashiotis et al., 2015). The same procedure was applied to the recording of the signal arising from a capillary containing solely the aqueous solution. Data were transformed to X-ray pair distribution function (PDF) data using PdfGetX3 (Juhas et al., 2013), with the contribution from the capillary and the aqueous solution being removed at this step. PDF data modelling was performed using PDFGui (Farrow et al., 2007). Turbostratic influences the PDF by attenuating the correlations resulting from pairs of atoms located on distinct layers as compared to those originating from atoms located on the same layer (Grangeon et al., 2015; Manceau et al., 2013). To circumvent this problem, the  $r$  interval of the simulation was restrained to the  $1.2\text{--}7.2\text{ \AA}$  range, i.e. to distances smaller than the layer-to-layer distance, using the model from Manceau and coworkers (Manceau et al., 2013). The atomic coordinates of  $^{\text{TC}}\text{Ni}$  and its coordination sphere were constrained from the qualitative analysis of PDF data (see below). During the modelling of the first PDF (collected on the sample before it was

contacted with  $\text{Ni}^{2+}$ ), the refined parameters were  $b$  (throughout the manuscript, data will be discussed in the frame of an orthogonal layer symmetry system – see below), the scale factor, the crystallite size (termed  $\text{spdiameter}$  in PDFGui), and the atomic correlated motion factor ( $\delta_2$  in PDFGui), as well as the occupancies of interlayer  $\text{Na}^+$  and  $^{55}\text{Mn}$ , the  $z$ -coordinates of interlayer  $\text{Na}^+$  and  $\text{H}_2\text{O}$  and thermal agitation factors. For these latter, two different set of values were refined: one for layer Mn, and one for the interlayer species ( $\text{Na}^+$  and  $\text{H}_2\text{O}$ ).  $u_{11}$  was equal to  $u_{22}$  in each of the two sets. Thermal agitation factor of layer O was set to two times that of layer Mn to conform with previous studies (Villalobos et al., 2006), and that of TC species was set to four times that of layer Mn, as suggested by STEM observation (see below). Because of the observed hexagonal layer symmetry (see below),  $a$  and  $b$  were linked, so that  $a = \sqrt{3} \times b$  ( $\gamma = 90^\circ$ ). The occupancy of interlayer  $\text{H}_2\text{O}$  was set to three times that of  $\text{Na}^+$  (Post and Veblen, 1990). The number of layer vacancies was set to one minus the sum of the occupancy of  $^{55}\text{Mn}$  plus one fourth that of  $\text{Na}^+$ . For all other PDF, collected during contact with  $\text{Ni}^{2+}$ , the occupancy of  $^{55}\text{Mn}$  was set equal to that obtained on the first sample, because it was previously shown that the occupancy of  $^{55}\text{Mn}$  remains constant regardless of  $^{55}\text{Ni}$  loading when equilibrium pH is acidic (Grangeon et al., 2008). Similarly, all atomic agitation factors were set equal to those obtained on the first sample, with those of  $^{55}\text{Ni}$  and  $^{55}\text{Mn}$  being set equal. The number of layer vacancies was constrained to be equal to one minus the sum of the occupancies of  $^{55}\text{Mn}$  plus half that of  $^{55}\text{Ni}$  plus one fourth that of  $\text{Na}^+$ . Thus, refinements were performed with only five free parameters. In all simulations, correlations between parameters remained below the threshold value (0.8) hard-coded in PDFGui. Note that as the set up imposed the use of relatively long ( $\sim 5$  cm) polyimide capillaries, a slight bending of this capillary could not be ruled out that would have influenced sample-to-detector distance and consequently refined lattice parameters.

Differential PDF were calculated after normalization of all PDF data to the correlation at  $2.86 \text{ \AA}$ , which is related to the shortest  $^{55}\text{Mn}$ – $^{55}\text{Mn}$  pair. A direct normalization by the incident photon flux failed, the overall intensity of the data changing with time due to a variable density of sample exposed to the beam, certainly because of compaction induced by the solution flow, or because of aggregation of particles.

Structure models obtained from PDF data modelling served as a basis for the calculation of XRD patterns using a modified version of the Calcpow program (Plancon, 2002), which is based on a matrix formalism capable of reproducing the effect of turbostratic (Drits et al., 2007) and which was previously applied to the study of phyllosilicates, layered double hydroxides, and phyllosulfates having various quantity of structural defects (Gates et al., 2002; Grangeon et al., 2016; Hadi et al., 2014; Manceau et al., 1997; Villalobos et al., 2006). The sole free parameters during this refinement were the size of the crystallites in the  $ab$  plane, the background, constrained to be similar to the one used to model the structure of other synthetic vernadite (Manceau et al., 2013), and microstrains which were modelled following this previous study, with the  $\delta$  parameter varying between 0.2 and 0.4. In these calculations, the isotropic temperature factors (B-factors) were set to  $0.5 \text{ \AA}^2$  for layer Mn,  $1 \text{ \AA}^2$  for layer O and  $2 \text{ \AA}^2$  for all other species.

### 2.3. Scanning transmission electron microscopy and electron energy loss spectroscopy

STEM and EELS analysis were carried out using a Cs-corrected Nion Ultra-STEM 200 operated at 100 kV. To increase the stability under the beam and to limit aggregation phenomena, samples were first embedded in epoxy resin and left 48 h in the dark for polymerization. The samples were then cut in slices of thickness  $\sim 50$  nm and deposited on a lacey carbon film loaded on copper grids. Images were acquired in high-angular annular dark-field (HAADF mode) and were simulated using QSTEM software (Koch, 2002).

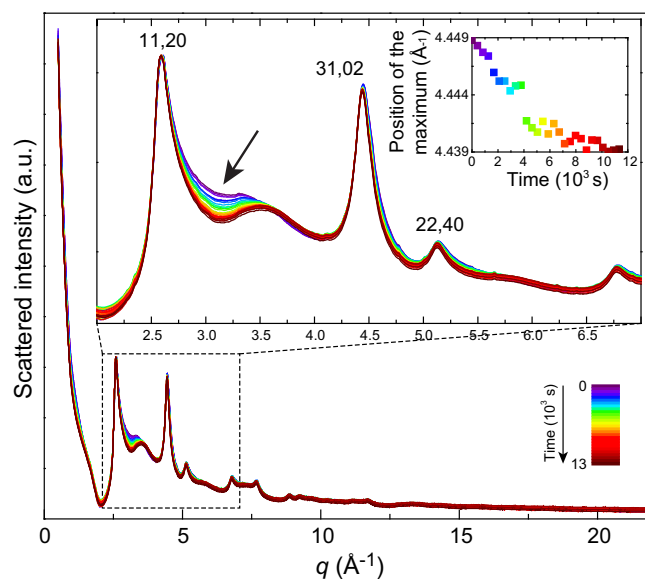


Fig. 2. Main panel shows all patterns collected during the experiment, after data processing and normalization to the maximum of the 11,20 reflection, to ease data comparison. Time increases in the order purple, blue, green, yellow, orange, red, and brown. Data delimited by the dotted square are enlarged in the top of the figure. Inset at the top right shows the evolution of the position of the maximum of the 31,02 band as a function of time. The arrow points out to the main change occurring as a function of time. (For interpretation of the references to colour in this figure legend, the reader is referred to the web version of this article.)

The EELS spectromicroscopy maps were obtained by collecting EELS spectra with spatial steps of 40 pm, acquisition times of 1 ms, energy ranges from 400 eV to 1000 eV and probe currents of 60 pA. In order to detect weak signal, the final EELS detector was an Electron Multiplying CCD that allows single electron sensitivity at 8 MHz read out speed.

## 3. Results and discussion

### 3.1. Qualitative study of XRD and PDF data

All XRD patterns collected as a function of time were typical for nanocrystalline turbostratic Mn oxide (Drits et al., 2007; Villalobos et al., 2006), all diffraction maxima being broad and some asymmetric with the intensity increasing sharply on the low  $q$  side and decreasing slowly on the high  $q$  side (Fig. 2). Crystallites were mainly built of isolated nanosheets, because no maxima could be observed at  $q \leq 2.1 \text{ \AA}^{-1}$  (equivalent to a  $d$ -spacing of  $3 \text{ \AA}$ ). Indeed, if the crystallites were built of more than  $\sim 1.5$  layers on average, a 001 reflection would be expressed at  $\sim 0.5 \text{ \AA}^{-1} \leq q \leq \sim 0.9 \text{ \AA}^{-1}$  (Grangeon et al., 2014; Lanson et al., 2008), as vernadite layer-to-layer distance usually varies between  $7 \text{ \AA}$  and  $10 \text{ \AA}$ .

The band at  $\sim 4.4 \text{ nm}^{-1}$  is indicative of the layer symmetry (Drits et al., 2007; Webb et al., 2005): it is almost symmetrical when layer symmetry is hexagonal, or split in two maxima when layer symmetry is orthogonal. It was symmetrical for our sample, and layer symmetry was thus hexagonal. Bands were indexed however with an orthogonal system ( $\gamma = 90^\circ$ ,  $a = \sqrt{3} \times b$ ) for consistency with previous studies (e.g. Drits et al., 2007; Villalobos et al., 2006). In this frame of reference, the maxima at  $2.59 \text{ \AA}^{-1}$  ( $2.43 \text{ \AA}$ ),  $4.45 \text{ \AA}^{-1}$  ( $1.41 \text{ \AA}$ ) and  $5.13 \text{ \AA}^{-1}$  ( $1.22 \text{ \AA}$ ) correspond to the 11,20, 31,02 and 22,40 bands, whose analysis is sufficient to determine the mean structure of vernadite, including the abundance of layer vacancies and TC species (Manceau et al., 2013).

The main changes observable in the patterns as a function of time – and thus of contact time with  $\text{Ni}^{2+}$  – lied in the high- $q$  side of the 11,20 band where diffracted intensity systematically decreased (arrow in Fig. 2), leading to the appearance and strengthening of a hump at



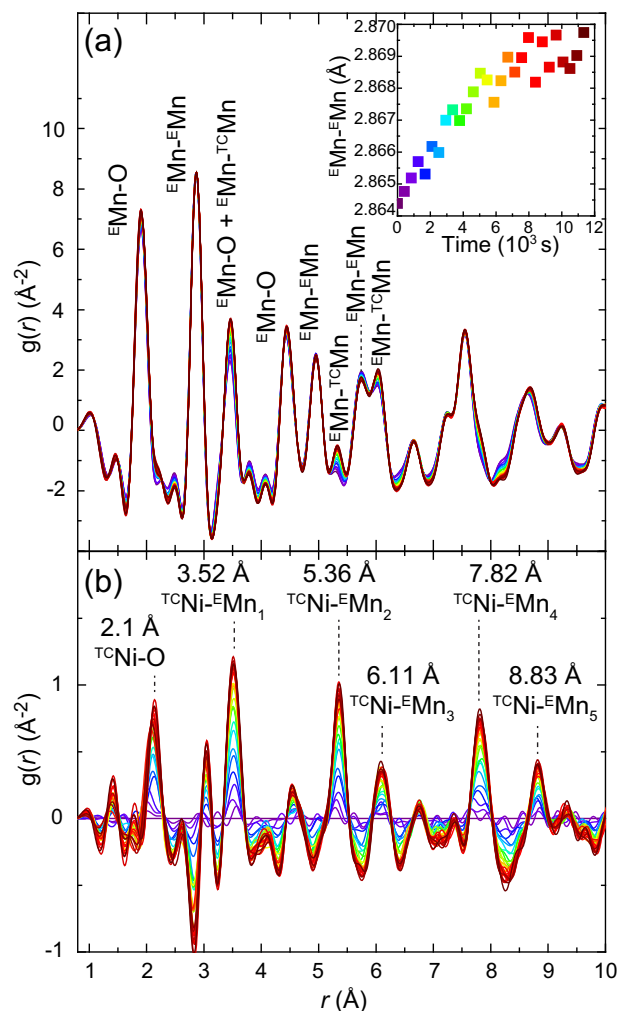


Fig. 3. (a): All PDF data collected during the experiment. Indexation is made for the first pattern, which corresponds to the sample before its interaction with  $\text{Ni}^{2+}$ . Inset shows the evolution of the position of the  $^{\text{E}}\text{Mn}-^{\text{E}}\text{Mn}$  correlation as a function of time. (b): d-PDF data, relative to the first PDF data. Colour scale as in Fig. 2.

$q \sim 3.55 \text{ \AA}^{-1}$  ( $1.77 \text{ \AA}$ ). Such modulation is a fingerprint for the presence of TC species (Grangeon et al., 2015; Lafferty et al., 2010) whose abundance, presumably  $^{\text{TC}}\text{Ni}$ , increased with time. Another systematic evolution of XRD patterns with time occurred on the 31,02 band whose position shifted from  $q = 4.45 \text{ \AA}^{-1}$  down to  $4.44 \text{ \AA}^{-1}$  after 11340 s (3.2 h) of contact time (Fig. 2). As this band is most sensitive to  $a$  and  $b$  (Lanson et al., 2008), it may be inferred that  $a$  and  $b$  lattice parameters increased with time.

As expected from the analysis of data in the reciprocal space, PDF data were representative of vernadite (Fig. 3a). The main correlations occurring at  $r$  lower than the usual layer-to-layer distance ( $\sim 7.2 \text{ \AA}$ ) and observable in the first pattern, which is representative of the sample before interaction with  $\text{Ni}^{2+}$ , are indexed in Fig. 3a (Grangeon et al., 2015; Manceau et al., 2013).

Upon contact of the sample with the solution, the PDF underwent time-dependent modifications, which were evinced using the differential PDF (d-PDF) data analysis method (Fig. 3b) previously used to investigate Cd and Pb sorption to vernadite (van Genuchten and Pena, 2016), and which consisted here in subtracting the first collected PDF signal to all other PDF signal. The d-PDF (Fig. 3b) evinced correlations that increased in intensity with time and that were attributable to  $^{\text{TC}}\text{Ni}-\text{O}$  and  $^{\text{TC}}\text{Ni}-^{\text{E}}\text{Mn}$  pairs according to qualitative examination of XRD patterns. Following previous studies (Manceau et al., 2007b; Peña et al., 2010; Simanova et al., 2015), the correlations at  $\sim 2.1 \text{ \AA}$  and  $3.52 \text{ \AA}$  were assumed to result from atomic pairs formed respectively by  $^{\text{TC}}\text{Ni}$

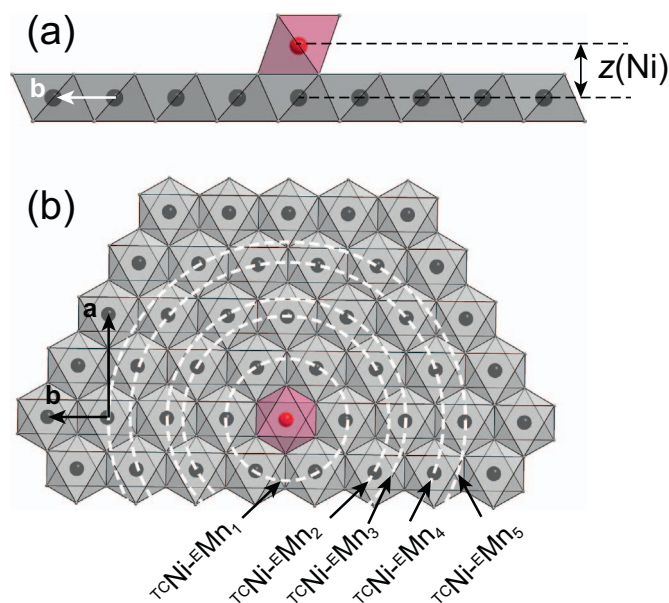


Fig. 4. Schematic representation of a  $^{\text{TC}}\text{Ni}$  atom (red dot) and its coordination sphere (red polyhedron) above a layer built of Mn atoms (black dots) in octahedral coordination (grey polyhedra). (a): View parallel to the layer plane ( $ab$  plane). (b): View perpendicular to the  $ab$  plane. Circles materialize the first  $^{\text{TC}}\text{Ni}-^{\text{E}}\text{Mn}$  shells. (For interpretation of the references to colour in this figure legend, the reader is referred to the web version of this article.)

and its O coordination sphere and by  $^{\text{TC}}\text{Ni}$  and the closest  $^{\text{E}}\text{Mn}$  atoms ( $^{\text{TC}}\text{Ni}-^{\text{E}}\text{Mn}_1$  distance – Fig. 4). Using this latter distance and the  $r$  value of the shortest  $^{\text{E}}\text{Mn}-^{\text{E}}\text{Mn}$  pair ( $\sim 2.87 \text{ \AA}$  – Fig. 3a) as  $b$ , the  $z$ -coordinate of the Ni atom [ $z(\text{Ni})$ ] above the plane formed by layer Mn atoms was  $2.05 \text{ \AA}$  (Fig. 4a). Using geometrical constraints imposed by the hexagonal layer symmetry, the position of the second, third, fourth and fifth  $^{\text{TC}}\text{Ni}-^{\text{E}}\text{Mn}$  correlations ( $^{\text{TC}}\text{Ni}-^{\text{E}}\text{Mn}_x$  pairs, where  $x = 2, 3, 4, 5$ ) could be predicted according to  $\sqrt{(z(\text{Ni})^2 + y^2)} \text{ \AA}$  where  $y = \sqrt{3} \times b$ ,  $2 \times b$ ,  $\sqrt{7} \times b$  and  $3 \times b$  (Fig. 4b), yielding respectively  $5.37 \text{ \AA}$ ,  $6.09 \text{ \AA}$ ,  $7.85 \text{ \AA}$ ,  $8.84 \text{ \AA}$ . The second, third, fourth and fifth correlations were indeed observed at  $5.36 \text{ \AA}$ ,  $6.11 \text{ \AA}$ ,  $7.82 \text{ \AA}$  and  $8.83 \text{ \AA}$ .

Finally, a weak correlation was observed at  $\sim 3.0 \text{ \AA}$ , on the high- $r$  side of the shortest  $^{\text{E}}\text{Mn}-^{\text{E}}\text{Mn}$  correlation. Its evolution was mirrored by a negative correlation at  $\sim 2.8 \text{ \AA}$ , on the low- $r$  side of the same  $^{\text{E}}\text{Mn}-^{\text{E}}\text{Mn}$  correlation. Consistent with XRD observations that lattice parameters increased with  $^{\text{TC}}\text{Ni}$  loading (Fig. 2), this behaviour resulted from a continuous shift of the first  $^{\text{E}}\text{Mn}-^{\text{E}}\text{Mn}$  correlation towards high  $r$  values with time (inset in Fig. 3a). Similar but weaker evolution was observed for the  $^{\text{E}}\text{Mn}-\text{O}$  correlation at  $4.45 \text{ \AA}$ , where a negative correlation at  $4.31 \text{ \AA}$  and a positive one at  $4.52 \text{ \AA}$  increased in intensity with time. At higher  $q$ , such evolution was not observed, suggesting that the layer deformations induced by  $^{\text{TC}}\text{Ni}$  only affected the local order. This assumption of local disorder is reinforced by the fact that the d-PDF at  $q > 10 \text{ \AA}^{-1}$  is dominated by  $^{\text{TC}}\text{Ni}-^{\text{E}}\text{Mn}$  correlations, demonstrating the presence of long-range order (Supplementary data Fig. S1).

### 3.2. Quantitative analysis of PDF data

To quantify  $^{\text{TC}}\text{Ni}$  as a function of time, the PDF were fitted using Manceau's model (Grangeon et al., 2015; Manceau et al., 2013; Supplementary Fig. S1 and Fig. 5).  $z(\text{Ni})$  was evaluated from the  $^{\text{TC}}\text{Ni}-^{\text{E}}\text{Mn}_3$  distance to limit the effect of local disorder. Consistently with qualitative observations (Figs. 2 and 3),  $^{\text{TC}}\text{Ni}$  increased with time, up to  $0.12 \pm 0.02$  per layer octahedron. The sorption mechanism underwent two regimes: up to  $\sim 5400 \text{ s}$  of contact time, the abundance of  $^{\text{TC}}\text{Ni}$  sharply increased from 0 to  $\sim 0.10$  per layer octahedron. Then, increase was much weaker, plateauing at  $\sim 0.12 \pm 0.02$   $^{\text{TC}}\text{Ni}$  per layer

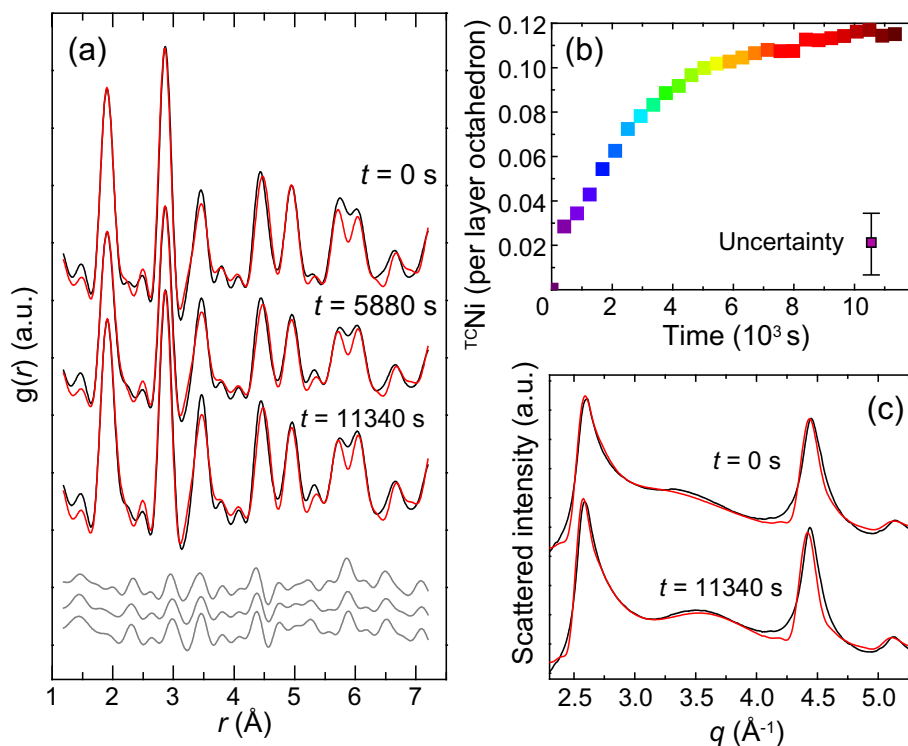


Fig. 5. (a) Selected experimental (black solid line) and calculated (red solid line) PDF: from top to bottom, contact time –  $t = 0$  s;  $R_{wp} = 18.3\%$ ,  $t = 5880$  s;  $R_{wp} = 17.3\%$ , and  $t = 11340$  s;  $R_{wp} = 17.9\%$ . The grey lines at the bottom are the residual fits, sorted from top to bottom. Simulation results for all PDF are available in the Supplementary Table S1; (b) Evolution of  $^{55}\text{Ni}$  as a function of time (colour as in Fig. 2); (c) Experimental data in the  $q$  space (black solid line), collected at  $t = 0$  s and at  $t = 11340$  s and comparison to patterns calculated using models obtained from PDF modelling (red solid line). (For interpretation of the references to colour in this figure legend, the reader is referred to the web version of this article.)

octahedron after  $\sim 11340$  s (3.2 h). The increase in lattice parameters evinced from the qualitative examination of both XRD and PDF data could not be quantified: although  $b$  steadily increased from  $2.8535 \pm 0.0021$  Å to  $2.8586 \pm 0.0018$  Å, this evolution remained mostly within uncertainties (see Supplementary Fig. S1). The equivalent isotropic B-factor of layer Mn was  $0.3$  Å<sup>2</sup>, close to the value of  $0.5$  Å<sup>2</sup> previously proposed (Lanson et al., 2008; Villalobos et al., 2006).

To further ensure that the  $1.2$ – $7.2$  Å range used for refinement was sufficient to accurately describe the layer structure at the crystallite scale, some models obtained from PDF modelling were used to calculate XRD patterns which were compared to experimental data (Fig. 5c). Given that no structure parameter was refined but the crystallite size in the  $ab$  plane, which was found to be  $6$  nm, the agreement between calculation and experiment was satisfying. In particular, the modulation of the high- $q$  side of the  $11,20$  band could be reproduced.

Using the Mn AOS of  $3.9$  obtained using potentiometric titration and results from PDF data modelling, the structural formula of the initial sample was determined to be  $^{55}\text{Mn}_{0.05}^{3+}\text{Na}_{0.23}^{+}(\text{H}_2\text{O})_{0.69}\text{H}_{0.06}^{+}[(\text{Mn}_{0.86}^{4+}\text{Mn}_{0.04}^{3+}\text{vac}_{0.1})\text{O}_2]$ , where species under brackets form the layer having “vac” layer vacancies, and where other species are present in the interlayer ( $\text{H}^{+}$  is adjusted to ensure charge compensation). The chemical formula of the sample obtained at the end of the experiment was deduced from the results of PDF modelling, assuming that the increase in the number of vacancies was due to the expulsion of layer  $\text{Mn}^{3+}$ , yielding  $^{55}\text{Ni}_{0.12}^{2+}\text{Mn}_{0.05}^{3+}\text{Na}_{0.12}^{+}\text{H}_{0.36}\text{H}_{0.01}^{+}[(\text{Mn}_{0.87}^{4+}\text{vac}_{0.13})\text{O}_2]$ . Mn AOS could not be measured because of a too low amount of sample in the capillary. It was assumed that the increase in the number of layer vacancies was due to the expulsion of layer  $\text{Mn}^{3+}$  because vacancies increased by  $0.03$  per layer octahedron as compared to the initial sample, close to the number of  $^{55}\text{Mn}^{3+}$  in the initial sample ( $0.04$ ). This possible expulsion of  $^{55}\text{Mn}^{3+}$  by  $^{55}\text{Ni}$ , which however remains speculative because of experimental and modelling uncertainties, is analogous to that evidenced for  $^{65}\text{Zn}$  (Grangeon et al., 2012), and is coherent with the

finding that sorption of  $^{55}\text{Ni}$  is accompanied by a decrease in  $^{55}\text{Mn}^{3+}$  (Grangeon et al., 2008).

### 3.3. Direct imaging of $\text{Ni}^{2+}$ sorption sites at vernadite surface

From the present data analysis,  $\text{Ni}^{2+}$  would mainly form  $^{55}\text{Ni}$ . However, identifying a minor amount of  $^{65}\text{Ni}$  in a vernadite sample containing mainly  $^{55}\text{Ni}$  is practically impossible using diffractometric methods, owing to the similarities of their local environments (Grangeon et al., 2008). In order to overcome this limitation, STEM-EELS analysis was employed (Fig. 6).

The systematic bending of the layers prevented crystals from being exactly perpendicular to the beam, and thus hampered the acquisition of atomic-resolution HAADF images of a whole crystal, explaining why, in Fig. 6, only part of the image has atomic-resolution. In this part where a slight distortion was visible, due to the strong bending near the surface and to sample drift, two types of atoms were distinguished on the basis of their relative brightness (inset of Fig. 6a).

The EELS analyses showed the presence of three absorption edges at  $\sim 530$  eV,  $\sim 640$  eV and  $\sim 855$  eV. The first one was assigned to the O K edge, while the second one clearly evinced the intense white line doublet from the Mn  $L_{2,3}$  edge. The last one corresponded to the Ni  $L_{2,3}$  edge and was only observed in areas that contained bright atoms (Fig. 6c), suggesting that bright atoms were Ni, whereas darker atoms were Mn. The STEM-HAADF images are often described as Z-contrast images with typically HAADF intensity considered to be proportional to  $Z^{1.6}$ . Such description cannot explain the difference of contrast observed in Fig. 6a, b for Mn ( $Z = 25$ ) and Ni ( $Z = 28$ ) atoms. Thermal diffuse scattering also plays a role in the HAADF intensity contrast and the origin of the stronger contrast of Ni with respect to Mn was thought to possibly result from a larger thermal agitation of  $^{55}\text{Ni}$  with respect to  $^{55}\text{Mn}$ . To test this hypothesis, STEM-HAADF calculations were performed using a model consisting of a vernadite layer with three vacancies, one being capped by

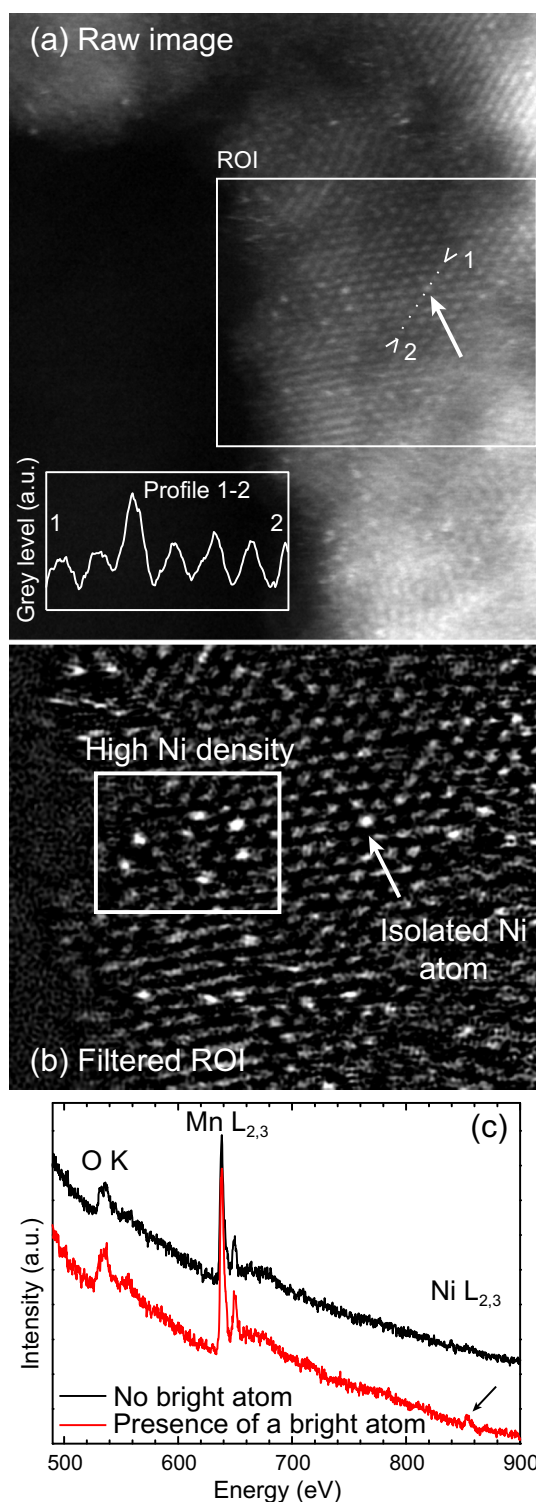


**Fig. 6.** (a) Raw HAADF image of synthetic vernadite crystals. The inset at the bottom left is a grey scale profile drawn along the dotted line shown in the main panel. It shows the presence of two types of atoms having different brightness. (b): Fourier-filtered image (over the  $1\text{--}13\text{ nm}^{-1}$  range) of the region of interest (ROI) delimited with a square in (a). Bright atoms are either relatively isolated from other bright atoms (arrow) or occur in regions of high density (square). The bright atom pointed out with an arrow is the same as that pointed out in (a). (c): Indexed EELS spectra acquired on regions containing bright atoms (red line) or no bright atom (black line). Only the EELS spectra acquired on areas containing bright atoms contain an Ni  $L_{2,3}$  edge (arrow). (For interpretation of the references to colour in this figure legend, the reader is referred to the web version of this article.)

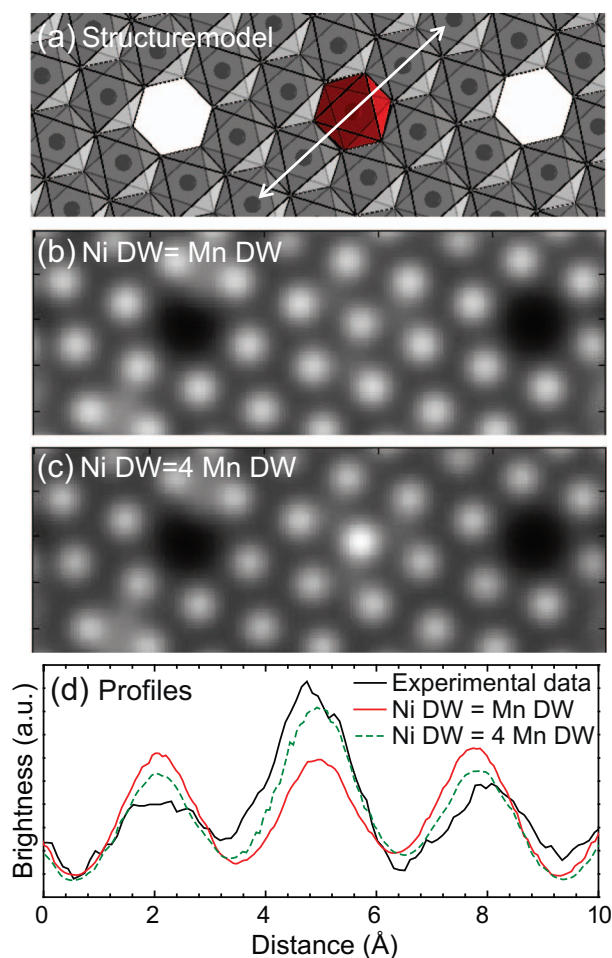


**Fig. 7.** (a): Structure model used for the calculation of a STEM-HAADF image. As in Fig. 4, black spheres and grey octahedra respectively materialize layer Mn atoms and their coordination sphere, while red spheres and red octahedra materialize  $^{\text{TC}}\text{Ni}$  and its coordination sphere. (b): Calculated image assuming that Mn and Ni Debye-Waller factors are both equal to  $0.5\text{ Å}^2$ . (c): Calculated image assuming that Mn and Ni Debye-Waller factors respectively are  $0.5\text{ Å}^2$  and  $2\text{ Å}^2$ . DW stands for “Debye-Waller factor”. (d): Grey profiles of scaled experimental data (black solid line; same as in Fig. 6) and of calculations shown in (b) (red solid line) and in (c) (green dotted line). For these two latter, the profile was drawn along the line with arrows in (a). (For interpretation of the references to colour in this figure legend, the reader is referred to the web version of this article.)

a  $^{\text{TC}}\text{Ni}$  (Figs. 4 and 7a). Images were calculated with a Debye-Waller coefficient of  $^{\text{TC}}\text{Ni}$  equivalent to the one of  $^{\text{E}}\text{Mn}$  or four times larger, i.e.  $0.5\text{ Å}^2$  or  $2\text{ Å}^2$  (Fig. 7b, c). The Ni atoms became brighter only for an agitation factor of  $2\text{ Å}^2$ . Furthermore, the intensity profile calculated for the largest agitation factors was in fair agreement with the experimental intensity (Fig. 7d), thus providing direct evidence for the higher thermal agitation factor of TC species as compared to that of  $^{\text{E}}\text{Mn}$ . Both STEM-EELS and STEM-HAADF confirmed the TC configuration of sorbed Ni.

Fig. 6a, b illustrates that Ni distribution within  $\delta\text{-MnO}_2$  structure was not ordered. Some regions contained Ni atoms which were only surrounded by Mn atoms over relatively long distances ( $\sim 1\text{ nm}$ ), whereas other regions were enriched in Ni. This, associated with the absence of  $^{\text{TC}}\text{Ni}$ - $^{\text{TC}}\text{Ni}$  correlation in the PDF, suggested that the ordered vacancies distribution previously observed on other samples (Manceau et al., 2013) is not systematic. Finally, a minor presence of  $^{\text{DC}}\text{Ni}$  was detected (top left of Fig. 6a). It was recently proposed that the abundance of  $^{\text{DC}}\text{Ni}$  depends on sample Mn AOS: when Mn AOS decreases from  $3.95 \pm 0.05$  down to  $3.65 \pm 0.05$ , the proportion of Ni at the edges of the crystals increases from 10–20% to about 80% (Simanova et al., 2015). Consistently, we could show that  $^{\text{DC}}\text{Ni}$  was a minor species when Mn AOS was 3.9.



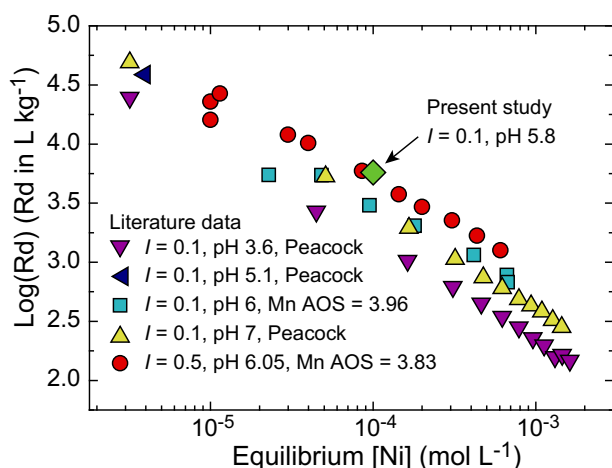


Fig. 8. Evolution of the Ni Rd as a function Ni concentration after equilibration, as reported by a number of previous studies materialized with triangle pointing to the bottom, left and top (Peacock and Sherman, 2007b), squares (Gray and Malati, 1979) and circles (Kanungo et al., 2004) and compared to presently obtained Rd (diamond). The size of the symbol corresponding to the present experiment has been chosen so that the vertical length matches the uncertainties on the abundance of  $^{55}\text{Ni}$ . Note that mean Mn oxidation degree was not reported by Peacock and Sherman (Peacock and Sherman, 2007b; datasets “Peacock”).

### 3.4. Implications

From values obtained on the adsorption plateau, the distribution coefficient  $R_D = 10^{3.76 \pm 0.06} \text{ L kg}^{-1}$  was calculated according to  $R_D = C_{\text{sorb}} / C_{\text{sol}}$ , where  $C_{\text{sorb}}$  is the Ni concentration on the solid (in  $\text{mol kg}^{-1}$ , deduced from PDF data modelling) and  $C_{\text{sol}}$  is the aqueous concentration of Ni. This  $R_D$  value was in close agreement with literature data obtained in similar conditions [Fig. 7;  $I = 0.1$ – $0.5$  vs.  $I = 0.1$  in the present study; pH values between 3.6 and 7 vs. 5.8 in the present study; mean Mn oxidation degree in the range 3.83 (Kanungo et al., 2004) to 3.96 (Gray and Malati, 1979; Gray et al., 1978) vs. 3.9 in the present study]. Consequently, our characterization method appears as a promising option to complement wet chemistry experiments. Indeed, the time-resolved PDF provides a direct insight in the structure of the solid, and allows determining the crystallographic sorption sites, with the main limitation that it cannot probe trace amounts of adsorbed species. Contrastingly, aqueous chemistry experiments make possible to probe very small changes in solution composition and thus to quantify adsorption processes over a wide range of aqueous metal concentrations, with the limitation that adsorption sites can only be interpreted in terms of sites density and affinity, without any possibility to attribute them to crystallographic sites.

According to literature data,  $R_D$  values depend weakly on pH (Fig. 8): at  $I = 0.1$ ,  $R_D$  increases by  $\sim 0.4$  log unit when pH increases from 3.6 to 7. This is consistent with our reactivity model in which an increased compensation by  $\text{H}^+$  of the charge associated with the O atoms forming a layer vacancy leads to a decrease in  $\text{Ni}^{2+}$  affinity for the surface, since  $\text{H}^+$  can compete with  $^{55}\text{Ni}$  (Peacock and Sherman, 2007b). A decrease in the mean manganese oxidation degree of the sample from 3.96 to 3.83, and thus an increase of the structural  $\text{Mn}^{3+}$  to  $\text{Mn}^{4+}$  ratio, leads to a slight increase of  $R_D$  value. This is also consistent with our model:  $^{55}\text{Ni}$  may adsorb above vacancies by replacing  $^{55}\text{Mn}^{3+}$  and adsorption of  $^{55}\text{Ni}$  is possibly accompanied by the release in solution of  $^{55}\text{Mn}^{3+}$ , thus generating new vacancies available for  $^{55}\text{Ni}$ . Consequently, a higher abundance of  $^{55}\text{Mn}^{3+}$  and (or)  $^{55}\text{Mn}^{3+}$  would improve vernadite adsorption reactivity towards  $\text{Ni}^{2+}$ .

In the presence of pH conditions that are relevant to many environmental systems such as soils,  $\text{Ni}^{2+}$  adsorbed mainly as  $^{55}\text{Ni}$ , and steady-state was reached after  $\sim 8000$  s ( $\sim 2$  h and 20 min) of

interaction. Such kinetic rate is, at least, one order of magnitude faster than those observed for adsorption at the surface of other soil minerals (pyrophyllite, talc, gibbsite, and silica - Scheckel and Sparks, 2001). This high adsorption kinetics rate, together with the high affinity of vernadite surface for  $\text{Ni}^{2+}$  and other trace metals explains why vernadite has been early described as a “scavenger” of trace metals (Goldberg, 1954).

### Notes

The authors declare no competing financial interest.

### Acknowledgements

S.G. acknowledges funding by the ANR (French National Research Agency; Project Nacre - ANR-14-CE01-0006). STEM experiments were performed at the LPS (Laboratoire de Physique des Solides, Orsay, France) in the frame of a research project granted by the national network for transmission electron microscopy and atom probe studies in France (METSAs). The HEXS experiments were performed on beamline ID22 at the European Synchrotron Radiation Facility (ESRF), Grenoble, France. We are grateful to Andy Fitch at the ESRF for providing assistance in using beamline ID22. This article benefited from comments and suggestions made by two anonymous reviewers.

### Appendix A. Supplementary data

The d-PDF data and assignment of  $^{55}\text{Ni}$ - $^{55}\text{Mn}$  correlations (Supplementary Fig. S1) up to  $r = 25$  Å and a list of parameters refined in all PDF data simulation procedures (Supplementary Table S1). Supplementary data associated with this article can be found in the online version, at doi:<http://dx.doi.org/10.1016/j.chemgeo.2017.03.035>.

### References

- Ashiotis, G., et al., 2015. The fast azimuthal integration Python library: pyFAI. *J. Appl. Crystallogr.* 48 (2), 510–519.
- Bargar, J.R., et al., 2009. Structural characterization of terrestrial microbial Mn oxides from Pinal Creek, AZ. *Geochim. Cosmochim. Acta* 73 (4), 889–910.
- Bodei, S., Manceau, A., Geoffroy, N., Baronnet, A., Buatier, M., 2007. Formation of todorokite from vernadite in Ni-rich hemipelagic sediments. *Geochim. Cosmochim. Acta* 71 (23), 5698–5716.
- Burns, R.G., Burns, V.M., 1977. Mineralogy of manganese nodules. In: Glasby, G.P. (Ed.), *Marine Manganese Deposits*. Elsevier, New York.
- Chukhrov, F.V., Sakharov, B.A., Gorshkov, A.I., Drits, V.A., Dikov, Y.P., 1985. Crystal structure of birnessite from the Pacific Ocean. *Int. Geol. Rev.* 27, 1082–1088.
- Dorn, R.L., 1991. Rock varnish. *Am. Sci.* 79 (6), 542–553.
- Dorn, R.L., Oberlander, T.M., 1981. Microbial origin of desert varnish. *Science* 213 (4513), 1245–1247.
- Dorn, R.L., et al., 1992. Manganese-rich rock varnish does occur in Antarctica. *Chem. Geol.* 99 (4), 289–298.
- Drits, V.A., Lanson, B., Gaillot, A.-C., 2007. Birnessite polytype systematics and identification by powder X-ray diffraction. *Am. Mineral.* 92 (5–6), 771–788.
- Exon, N.F., Raven, M.D., De Carlo, E.H., 2002. Ferromanganese nodules and crusts from the Christmas Island region, Indian Ocean. *Mar. Georesour. Geotechnol.* 20 (4), 275–297.
- Farrow, C., et al., 2007. PDFfit2 and PDFgui: computer programs for studying nanostructure in crystals. *J. Phys. Condens. Matter* 19 (33), 335219.
- Fuller, C.C., Bargar, J.R., 2014. Processes of zinc attenuation by biogenic manganese oxides forming in the hyporheic zone of Pinal Creek, Arizona. *Environ. Sci. Technol.* 48 (4), 2165–2172.
- Gates, W.P., Slade, P.G., Manceau, A., Lanson, B., 2002. Site occupancies by iron in nontronites. *Clay Clay Miner.* 50 (2), 223–239.
- van Genuchten, C.M., Pena, J., 2016. Sorption selectivity of birnessite particle edges: a d-PDF analysis of Cd(II) and Pb(II) sorption by  $\delta$ - $\text{MnO}_2$  and ferrihydrite. *Environ. Sci. Process. Impacts* 18, 1030–1041.
- Giovanoli, R., 1980. Vernadite is random-stacked birnessite. *Mineral. Deposita* 15, 251–253.
- Glover, E.D., 1977. Characterization of a marine birnessite. *Am. Mineral.* 62 (3–4), 278–285.
- Goldberg, E.D., 1954. Marine geochemistry 1. Chemical scavengers of the sea. *J. Geol.* 62 (3), 249–265.
- Grangeon, S., Lanson, B., Lanson, M., Manceau, A., 2008. Crystal structure of Ni-sorbed synthetic vernadite: a powder X-ray diffraction study. *Mineral. Mag.* 72 (6),



- 1197–1209.
- Grangeon, S., Lanson, B., Miyata, N., Tani, Y., Manceau, A., 2010. Structure of nanocrystalline phyllosilicates produced by freshwater fungi. *Am. Mineral.* 95 (11–12), 1608–1616.
- Grangeon, S., et al., 2012. Zn sorption modifies dynamically the layer and interlayer structure of vernadite. *Geochim. Cosmochim. Acta* 85 (9), 302–313.
- Grangeon, S., Lanson, B., Lanson, M., 2014. Solid-state transformation of nanocrystalline phyllosilicate into tectomanganate: influence of initial layer and interlayer structure. *Acta Crystallogr. Sect. B: Struct. Sci. Cryst. Eng. Mater.* 70, 828–838.
- Grangeon, S., et al., 2015. Cryptomelane formation from nanocrystalline vernadite precursor: a high energy X-ray scattering and transmission electron microscopy perspective on reaction mechanisms. *Geochim. Trans.* 16.
- Grangeon, S., et al., 2016. Structure of nanocrystalline calcium silicate hydrates: insights from X-ray diffraction, synchrotron X-ray absorption and nuclear magnetic resonance. *J. Appl. Crystallogr.* 49, 771–783.
- Gray, M.J., Malati, M.A., 1979. Adsorption from aqueous solution by d-manganese dioxide II. Adsorption of some heavy metal cations. *J. Chem. Technol. Biotechnol.* 29 (3), 135–144.
- Gray, M.J., Malati, M.A., Rophael, M.W., 1978. The point of zero charge of manganese dioxides. *J. Electroanal. Chem. Interfacial Electrochem.* 89 (1), 135–140.
- Hadi, J., Grangeon, S., Warmont, F., Seron, A., Greneche, J.-M., 2014. A novel and easy chemical-clock synthesis of nanocrystalline iron–cobalt bearing layered double hydroxides. *J. Colloid Interface Sci.* 434 (0), 130–140.
- Hastings, D., Emerson, S., 1986. Oxidation of manganese by spores of a marine bacillus: kinetic and thermodynamic considerations. *Geochim. Cosmochim. Acta* 50 (8), 1819–1824.
- Juhas, P., Davis, T., Farrow, C.L., Billinge, S.J.L., 2013. PDFgetX3: a rapid and highly automatable program for processing powder diffraction data into total scattering pair distribution functions. *J. Appl. Crystallogr.* 46 (2), 560–566.
- Kanungo, S.B., Tripathy, S.S., Mishra, S.K., Sahoo, B., Rajeev, 2004. Adsorption of  $\text{Co}^{2+}$ ,  $\text{Ni}^{2+}$ ,  $\text{Cu}^{2+}$ , and  $\text{Zn}^{2+}$  onto amorphous hydrous manganese dioxide from simple (1–1) electrolyte solutions. *J. Colloid Interface Sci.* 269 (1), 11–21.
- Kasprzak, K.S., Sunderman, F.W., Salnikow, K., 2003. Nickel carcinogenesis. *Mutat. Res. Fundam. Mol. Mech. Mutagen.* 533 (1–2), 67–97.
- Koch, C., 2002. Determination of Core Structure Periodicity and Point Defect Density Along Dislocations.
- Koschinsky, A., Halbach, P., 1995. Sequential leaching of marine ferromanganese precipitates: genetic implications. *Geochim. Cosmochim. Acta* 59 (24), 5113–5132.
- Lafferty, B.J., Ginder-Vogel, M., Zhu, M., Livi, K.J.T., Sparks, D.L., 2010. Arsenite oxidation by a poorly crystalline manganese-oxide. 2. Results from X-ray absorption spectroscopy and X-ray diffraction. *Environ. Sci. Technol.* 44 (22), 8467–8472.
- Lanson, B., Drits, V.A., Silvester, E., Manceau, A., 2000. Structure of H-exchange hexagonal birnessite and its mechanism of formation from Na-rich monoclinic busierite at low pH. *Am. Mineral.* 85 (5–6), 826–838.
- Lanson, B., Drits, V.A., Feng, Q., Manceau, A., 2002a. Structure of synthetic Na-birnessite: evidence for a triclinic one-layer unit cell. *Am. Mineral.* 87 (11–12), 1662–1671.
- Lanson, B., et al., 2002b. Structure of heavy-metal sorbed birnessite: part 1. Results from X-ray diffraction. *Am. Mineral.* 87 (11–12), 1631–1645.
- Lanson, B., et al., 2008. Formation of Zn-Ca phyllosilicate nanoparticles in grass roots. *Geochim. Cosmochim. Acta* 72 (10), 2478–2490.
- Lopano, C.L., Heaney, P.J., Post, J.E., 2009. Cs-exchange in birnessite: reaction mechanisms inferred from time-resolved X-ray diffraction and transmission electron microscopy. *Am. Mineral.* 94 (5–6), 816–826.
- Lopano, C.L., Heaney, P.J., Bandstra, J.Z., Post, J.E., Brantley, S.L., 2011. Kinetic analysis of cation exchange in birnessite using time-resolved synchrotron X-ray diffraction. *Geochim. Cosmochim. Acta* 75 (14), 3973–3981.
- Manceau, A., Drits, V.A., Silvester, E., Bartoli, C., Lanson, B., 1997. Structural mechanism of  $\text{Co}^{2+}$  oxidation by the phyllosilicate busierite. *Am. Mineral.* 82 (11–12), 1150–1175.
- Manceau, A., et al., 2000. Quantitative Zn speciation in smelter-contaminated soils by EXAFS spectroscopy. *Am. J. Sci.* 300 (4), 289–343.
- Manceau, A., et al., 2003. Molecular-scale speciation of Zn and Ni in soil ferromanganese nodules from loess soils of the Mississippi Basin. *Environ. Sci. Technol.* 37 (1), 75–80.
- Manceau, A., et al., 2004. Natural speciation of Zn at the micrometer scale in a clayey soil using X-ray fluorescence, absorption, and diffraction. *Geochim. Cosmochim. Acta* 68 (11), 2467–2483.
- Manceau, A., Kersten, M., Marcus, M.A., Geoffroy, N., Granina, L., 2007a. Ba and Ni speciation in a nodule of binary Mn oxide phase composition from Lake Baikal. *Geochim. Cosmochim. Acta* 71 (8), 1967–1981.
- Manceau, A., Lanson, M., Geoffroy, N., 2007b. Natural speciation of Ni, Zn, Ba, and As in ferromanganese coatings on quartz using X-ray fluorescence, absorption, and diffraction. *Geochim. Cosmochim. Acta* 71 (1), 95–128.
- Manceau, A., et al., 2013. Short-range and long-range order of phyllosilicate nanoparticles determined using high-energy X-ray scattering. *J. Appl. Crystallogr.* 46 (1), 193–209.
- Manceau, A., Lanson, M., Takahashi, Y., 2014. Mineralogy and crystal chemistry of Mn, Fe, Co, Ni, and Cu in a deep-sea Pacific polymetallic nodule. *Am. Mineral.* 99 (10), 2068–2083.
- Marcus, M.A., Manceau, A., Kersten, M., 2004. Mn, Fe, Zn and As speciation in a fast-growing ferromanganese marine nodule. *Geochim. Cosmochim. Acta* 68 (14), 3125–3136.
- Marty, N.C.M., Grangeon, S., Warmont, F., Lerouge, C., 2015. Alteration of nanocrystalline calcium silicate hydrate (C-S-H) at pH 9.2 and room temperature: a combined mineralogical and chemical study. *Mineral. Mag.* 79 (2), 437–458.
- Nicholson, F.A., Smith, S.R., Alloway, B.J., Carlton-Smith, C., Chambers, B.J., 2003. An inventory of heavy metals inputs to agricultural soils in England and Wales. *Sci. Total Environ.* 311 (1–3), 205–219.
- Palumbo, B., Bellanca, A., Neri, R., Roe, M.J., 2001. Trace metal partitioning in Fe-Mn nodules from Sicilian soils, Italy. *Chem. Geol.* 173 (4), 257–269.
- Peacock, C.L., 2009. Physicochemical controls on the crystal-chemistry of Ni in birnessite: genetic implications for ferromanganese precipitates. *Geochim. Cosmochim. Acta* 73 (12), 3568–3578.
- Peacock, C.L., Moon, E.M., 2012. Oxidative scavenging of thallium by birnessite: explanation for thallium enrichment and stable isotope fractionation in marine ferromanganese precipitates. *Geochim. Cosmochim. Acta* 84 (0), 297–313.
- Peacock, C.L., Sherman, D.M., 2007a. Crystal-chemistry of Ni in marine ferromanganese crusts and nodules. *Am. Mineral.* 92 (7), 1087–1092.
- Peacock, C.L., Sherman, D.M., 2007b. Sorption of Ni by birnessite: equilibrium controls on Ni in seawater. *Chem. Geol.* 238 (1–2), 94–106.
- Peña, J., Kwon, K.D., Refson, K., Bargar, J.R., Sposito, G., 2010. Mechanisms of nickel sorption by a bacteriogenic birnessite. *Geochim. Cosmochim. Acta* 74 (11), 3076–3089.
- Peña, J., Bargar, J.R., Sposito, G., 2015. Copper sorption by the edge surfaces of synthetic birnessite nanoparticles. *Chem. Geol.* 396 (0), 196–207.
- Plancon, A., 2002. CALCIPOW: a program for calculating the diffraction by disordered lamellar structures. *J. Appl. Crystallogr.* 35 (3), 377.
- Post, J.E., Veblen, D.R., 1990. Crystal structure determinations of synthetic sodium, magnesium, and potassium birnessite using TEM and the Rietveld method. *Am. Mineral.* 75 (5–6), 477–489.
- Potter, R.M., Rossman, G.R., 1979. The manganese- and iron-oxide mineralogy of desert varnish. *Chem. Geol.* 25 (1–2), 79–94.
- Scheckel, K.G., Sparks, D.L., 2001. Temperature effects on nickel sorption kinetics at the mineral–water interface. *Soil Sci. Soc. Am. J.* 65 (3), 719–728.
- Simanova, A.A., et al., 2015. Probing the sorption reactivity of the edge surfaces in birnessite nanoparticles using nickel(II). *Geochim. Cosmochim. Acta* 164, 191–204.
- Takahashi, Y., Manceau, A., Geoffroy, N., Marcus, M.A., Usui, A., 2007. Chemical and structural control of the partitioning of Co, Ce, and Pb in marine ferromanganese oxides. *Geochim. Cosmochim. Acta* 71 (4), 984–1008.
- Tani, Y., et al., 2003. Biogeochemistry of manganese oxide coatings on pebble surfaces in the Kikukawa River System, Shizuoka, Japan. *Appl. Geochem.* 18 (10), 1541–1554.
- Tebo, B.M., et al., 2004. Biogenic manganese oxides: properties and mechanisms of formation. *Annu. Rev. Earth Planet. Sci.* 32 (1), 287–328.
- Tonkin, J.W., Balistrieri, L.S., Murray, J.W., 2004. Modeling sorption of divalent metal cations on hydrous manganese oxide using the diffuse double layer model. *Appl. Geochem.* 19 (1), 29–53.
- Villalobos, M., Toner, B., Bargar, J., Sposito, G., 2003. Characterization of the manganese oxide produced by *Pseudomonas putida* strain MnB1. *Geochim. Cosmochim. Acta* 67, 2649–2662.
- Villalobos, M., Lanson, B., Manceau, A., Toner, B., Sposito, G., 2006. Structural model for the biogenic Mn oxide produced by *Pseudomonas putida*. *Am. Mineral.* 91 (4), 489–502.
- Wang, D., Wang, Y., 2008. Nickel sulfate induces numerous defects in *Caenorhabditis elegans* that can also be transferred to progeny. *Environ. Pollut.* 151 (3), 585–592.
- Webb, S.M., Tebo, B.M., Bargar, J.R., 2005. Structural characterization of biogenic Mn oxides produced in seawater by the marine *Bacillus* sp. strain SG-1. *Am. Mineral.* 90 (8–9), 1342–1357.
- Wegorzewski, A.V., Kuhn, T., Dohrmann, R., Wirth, R., Grangeon, S., 2015. Mineralogical characterization of individual growth structures of Mn-nodules with different Ni plus Cu content from the central Pacific Ocean. *Am. Mineral.* 100 (11–12), 2497–2508.
- Weng, L.P., Wolthoorn, A., Lexmond, T.M., Temminghoff, E.J.M., van Riemsdijk, W.H., 2004. Understanding the effects of soil characteristics on phytotoxicity and bioavailability of nickel using speciation models. *Environ. Sci. Technol.* 38 (1), 156–162.